



## Network design for quantifying urban CO<sub>2</sub> emissions: Assessing trade-offs between precision and network density

Alexander J. Turner<sup>1</sup>, Alexis A. Shusterman<sup>2</sup>, Brian C. McDonald<sup>3,\*</sup>,  
Virginia Teige<sup>2</sup>, Robert A. Harley<sup>3</sup>, and Ronald C. Cohen<sup>2,4</sup>

<sup>1</sup>School of Engineering and Applied Sciences, Harvard University, Cambridge, Massachusetts, USA.

<sup>2</sup>Department of Chemistry, University of California at Berkeley, Berkeley, CA, USA.

<sup>3</sup>Department of Civil and Engineering, University of California at Berkeley, Berkeley, CA, USA.

<sup>4</sup>Department of Earth and Planetary Sciences, University of California at Berkeley, Berkeley, CA, USA.

\*now at: Cooperative Institute for Research in Environmental Sciences, University of Colorado Boulder, Boulder, Colorado, USA.

*Correspondence to:* Ronald C. Cohen  
(rccohen@berkeley.edu)

1 **Abstract.** The majority of anthropogenic CO<sub>2</sub> emissions are attributable to urban areas. While  
2 the emissions from urban electricity generation often occur in locations remote from consumption,  
3 many of the other emissions occur within the city limits. Evaluating the effectiveness of strategies  
4 for controlling these emissions depends on our ability to observe urban CO<sub>2</sub> emissions and attribute  
5 them to specific activities. Cost effective strategies for doing so have yet to be described. Here we  
6 characterize the ability of a prototype measurement network, modeled after the BEACO<sub>2</sub>N network,  
7 in combination with an inverse model based on WRF-STILT to improve our understanding of urban  
8 emissions. The pseudo-measurement network includes 34 sites at roughly 2 km spacing covering  
9 an area of roughly 400 km<sup>2</sup>. The model uses an hourly 1×1 km<sup>2</sup> emission inventory and 1×1  
10 km<sup>2</sup> meteorological calculations. We perform an ensemble of Bayesian atmospheric inversions to  
11 sample the combined effects of uncertainties of the pseudo-measurements and the model. We vary  
12 the estimates of the combined uncertainty of the pseudo-observations and model over a range of 20  
13 ppm to 0.005 ppm and vary the number of sites from 1 to 34. We use these inversions to develop  
14 statistical models that estimate the efficacy of the combined model-observing system at reducing  
15 uncertainty in CO<sub>2</sub> emissions. We examine uncertainty in estimated CO<sub>2</sub> fluxes at the urban scale,  
16 as well as for sources embedded within the city such as a line source (e.g., a highway) or a point  
17 source (e.g., emissions from the stacks of small industrial facilities). We find that a dense network  
18 with moderate precision is the preferred setup for estimating area, line, and point sources from  
19 a combined uncertainty and cost perspective. The dense network considered here could estimate



20 weekly CO<sub>2</sub> emissions from an urban region with less than 5% error, given our characterization of  
21 the combined observation and model uncertainty.

## 22 1 Introduction

23 Carbon dioxide (CO<sub>2</sub>) is an atmospheric trace gas and the single largest anthropogenic radiative  
24 forcer, with a radiative forcing of 1.82 W m<sup>-2</sup> since preindustrial times (IPCC, 2013). CO<sub>2</sub> has  
25 increased from 280 ppm in preindustrial times to greater than 400 ppm in the present, largely due  
26 to changes in fossil fuel emissions. Over 70% of these fossil fuel CO<sub>2</sub> emissions in the United  
27 States (US) are attributable to urban areas (EIA, 2015; Hutyra et al., 2014). As such, quantifying  
28 and monitoring the emissions from urban areas is crucial to strategies for reducing future increases  
29 in CO<sub>2</sub>.

30 Numerous studies have performed top-down estimations of CO<sub>2</sub> emissions using observations  
31 from urban surface monitoring networks of various sizes (e.g., Gratani and Varone, 2005; McKain  
32 et al., 2012; Newman et al., 2013; Lauvaux et al., 2013; Breon et al., 2015; Turnbull et al., 2015).  
33 However, it's not immediately clear how many sites are necessary to monitor the emissions from an  
34 urban area. Kort et al. (2013) found that a surface monitoring network would need at least 8 sites  
35 operating for 8 weeks to accurately estimate CO<sub>2</sub> emissions in Los Angeles. Yet most current urban  
36 monitoring networks have fewer than 8 sites but operate for much longer than 8 weeks. For example,  
37 Gratani and Varone (2005) used a single site in Rome, Newman et al. (2013) used a single site in  
38 Los Angeles, Lauvaux et al. (2013) used two sites in Davos, Switzerland, McKain et al. (2012) used  
39 a network of 5 sites in Salt Lake City, and Breon et al. (2015) used 5 sites in Paris. Recent work  
40 from Turnbull et al. (2015) employed a denser network of 12 sites in Indianapolis.

41 This issue is further complicated by bias and noise in both the measurements and the modeling  
42 framework. The combined model and measurement error is known as the model-data mismatch error  
43 (hereafter referred to as the "mismatch error"). Current monitoring networks use a mix of instru-  
44 ments and approaches to calibration with resulting variations of capital and operating costs, network  
45 precision, and potential instrument bias. Monitoring networks located in regions with complex orog-  
46 raphy are challenging for atmospheric transport calculations, making it more difficult to determine  
47 the dispersion from sources.

48 The tradeoff between measurement network density and mismatch error has yet to be charac-  
49 terized. Understanding these tradeoffs is crucial to reducing the uncertainty in emissions from ur-  
50 ban regions and to developing cost-effective urban monitoring networks. Here we present a high-  
51 resolution inventory of CO<sub>2</sub> fluxes and a numerical model that relates atmospheric observations to  
52 high resolution surface fluxes. We then use this inventory and model in a series of observing system  
53 simulation experiments (OSSEs) to investigate the tradeoff between reductions in the mismatch error  
54 and increases in the measurement network density. We develop statistical models to characterize this



55 relationship for different types of sources in the San Francisco Bay Area, identify limiting regimes,  
56 and recommend future observing strategies.

## 57 **2 Constructing a high resolution regional CO<sub>2</sub> inventory**

58 McDonald et al. (2014) demonstrated that  $1 \times 1 \text{ km}^2$  spatial resolution is necessary to resolve the  
59 gradients in urban CO<sub>2</sub> fluxes from highways. However, most of the existing CO<sub>2</sub> anthropogenic  
60 inventories are not available at this resolution. For example, EDGAR (European Commission, 2011)  
61 and VULCAN (Gurney et al., 2009) are only available at  $0.1^\circ \times 0.1^\circ$  and  $10 \times 10 \text{ km}^2$ , respectively.  
62 A notable exception is the Odiac fossil fuel CO<sub>2</sub> inventory (Oda and Maksyutov, 2011) which is  
63 based on satellite-observed nightlight data and available globally at  $1 \times 1 \text{ km}^2$  resolution. High reso-  
64 lution fossil fuel CO<sub>2</sub> emissions are available for select cities and sectors such as Paris through the  
65 AirParif inventory (Breon et al., 2015, <http://www.airparif.asso.fr/en/index/index>) and Indianapo-  
66 liss, Los Angeles, Salt Lake City, and Phoenix through the HESTIA project (Gurney et al., 2012,  
67 <http://hestia.project.asu.edu/>); three recent studies (Gately et al., 2013; McDonald et al., 2014; Gately  
68 et al., 2015) developed high resolution CO<sub>2</sub> emissions from vehicular traffic.

69 The Bay Area Air Quality Management District (BAAQMD) provides detailed county-level CO<sub>2</sub>  
70 emissions information for San Francisco and California's Bay Area (Mangat et al., 2010). The  
71 BAAQMD found that the transportation sector accounted for 36% of the Bay Area anthropogenic  
72 emissions, industrial and commercial for 36%, electricity for 16%, residential fuel usage for 7%,  
73 off-road equipment for 3.0%, and agriculture for 1%. The BAAQMD also reports CO<sub>2</sub> emissions  
74 for 4,375 point sources in the Bay Area. We geocode these point sources based on the addresses pro-  
75 vided by the BAAQMD. These point sources capture the emissions from the industrial, commercial,  
76 and electricity sectors. We map residential fuel usage to population using block level population  
77 data from the 2010 US Census and apply a temporal temperature scaling based on Deschnes and  
78 Greenstone (2011); the resulting temporal scaling effect is small due to the temperate climate in the  
79 East Bay region of the SF Bay Area.

80 Here we use the traffic CO<sub>2</sub> emissions from the fuel-based inventory for vehicle emissions (FIVE)  
81 developed by McDonald et al. (2014). The FIVE traffic CO<sub>2</sub> inventory provides a representative  
82 week of hourly CO<sub>2</sub> emissions for San Francisco and other nearby Bay Area cities at 10 km, 4  
83 km, 1 km, and 500 m resolution. The FIVE inventory is constructed by partitioning CO<sub>2</sub> emissions  
84 using state-level fuel data to individual roads with road-specific traffic count data and temporal pat-  
85 terns from weigh-in-motion data. In this manner, CO<sub>2</sub> emissions from the FIVE inventory will be  
86 consistent with state and national CO<sub>2</sub> budgets and can easily be scaled to different years.

87 Combining the industrial, commercial, electricity, residential, and traffic emissions account for  
88 95.8% of the anthropogenic CO<sub>2</sub> emissions in the Bay Area. We do not have high resolution proxy  
89 data for the off-road equipment or agriculture sectors in the Bay Area and have chosen to assume



90 their contributions are smaller than the uncertainty in the total budget; therefore we neglect these  
91 sectors in the construction of our inventory.

92 CarbonTracker CT2013B (<http://www.esrl.noaa.gov/gmd/ccgg/carbontracker/>; Peters et al., 2007)  
93 provides 3 hourly fossil fuel, ocean, biogenic, and fire CO<sub>2</sub> fluxes at 1° × 1° resolution. These fluxes  
94 are optimized to agree with atmospheric CO<sub>2</sub> observations. We regrid these fluxes to 1 × 1 km<sup>2</sup>  
95 spatial resolution and use the fire, ocean, and biogenic sectors to account for our natural fluxes.

96 Fig. 1 shows snapshots of the CO<sub>2</sub> fluxes from our inventory at 4 different times of day and  
97 the a-temporal fluxes from EDGAR v4.2 FT2010 (European Commission, 2011). From Fig. 1 we  
98 can see the inventory clearly resolves the large CO<sub>2</sub> gradients from highways, confirming that 1 × 1  
99 km<sup>2</sup> spatial resolution is sufficient to resolve urban CO<sub>2</sub> fluxes from highways. The bottom panel  
100 of Fig. 1 shows a time series of Bay Area CO<sub>2</sub> fluxes broken down by source. The diurnal cycle  
101 in our inventory is largely driven by the traffic emissions with modest uptake from the biosphere  
102 during the middle of the day. Other anthropogenic sources were assumed to have a negligible diurnal  
103 cycle (Nassar et al., 2013). In what follows, we use EDGAR as the prior and the high spatio-temporal  
104 resolution inventory as the “truth”.

105 [Fig. 1 about here.]

### 106 3 The Berkeley Atmospheric CO<sub>2</sub> Observation Network (BEACO<sub>2</sub>N)

107 The Berkeley Atmospheric CO<sub>2</sub> Observation Network (“BEACO<sub>2</sub>N”, see <http://beacon.berkeley.edu>)  
108 was founded in 2012 as a web of approximately 25 carbon dioxide sensing “nodes” stationed atop  
109 schools and museums in the Oakland, CA metropolitan area (see Table 1). With sensors installed on  
110 an approximately 2 km square grid, BEACO<sub>2</sub>N is the only surface-level (3 to 130 m a.g.l.) green-  
111 house gas monitoring system with roughly the same spatial resolution as the emissions inventories  
112 described above. Each node requires only a standard, 120V power source and is sited on pre-existing  
113 structures based on voluntary, no-cost partnerships. The BEACO<sub>2</sub>N configuration therefore repre-  
114 sents a reasonable expectation and is one model for future monitoring networks aimed at constraining  
115 CO<sub>2</sub> fluxes at neighborhood scales within an urban dome.

116 [Table 1 about here.]

117 BEACO<sub>2</sub>N’s unprecedented spatial density is achieved by exploiting lower cost instrumentation  
118 than has traditionally been utilized for ambient CO<sub>2</sub> detection. The non-dispersive infrared (NDIR)  
119 absorption sensor used in each BEACO<sub>2</sub>N node (<http://www.vaisala.com/en/products/carbondioxide/Pages/GMP343.aspx>)  
120 has been seen to possess adequate sensitivity to resolve diurnal as well as seasonal phenomena rele-  
121 vant to urban environments (Rigby et al., 2008) and costs one to two orders of magnitude less than  
122 the commercial cavity ring-down instruments commonly used in other networks. However, the low-  
123 cost NDIR sensor is more susceptible to factors such as temporal drift and environmental instability





124 that can negatively impact data quality. This trade-off between mismatch error and network density  
125 is explored below.

#### 126 4 Observing system simulation experiments

127 CO<sub>2</sub> concentrations were simulated at 34 sites in the BEACO<sub>2</sub>N network with the Stochastic Time-  
128 Inverted Lagrangian Transport (STILT) model (Lin et al., 2003), coupled to the Weather Research  
129 and Forecasting (WRF) meso-scale meteorological model run at 1×1 km<sup>2</sup> grid resolution (WRF-  
130 STILT; Nehrkorn et al., 2010). WRF-STILT computes footprints (Δ CO<sub>2</sub> per surface flux, or ppm  
131 per μmol·m<sup>-2</sup>·s<sup>-1</sup>) for each observation that relate the CO<sub>2</sub> fluxes ( $\mathbf{x}$ ; an  $m \times 1$  vector) to the  
132 observations ( $\mathbf{y}$ ; an  $n \times 1$  vector):

$$133 \quad \mathbf{y} = \mathbf{H}\mathbf{x} \quad (1)$$

134 Each row of the  $n \times m$  Jacobian matrix ( $\mathbf{H} = \partial\mathbf{y}/\partial\mathbf{x}$ ) is a reshaped footprint. Fig. 2 shows the  
135 location of the sites and the average network footprint for Sept 15 to 22.

136 [Fig. 2 about here.]

137 Here we use our high resolution CO<sub>2</sub> inventory ( $\mathbf{x}^a$ ; an  $m \times 1$  vector) to generate synthetic obser-  
138 vations ( $\mathbf{y}^a$ ; an  $n \times 1$  vector):

$$139 \quad \mathbf{y}^a = \mathbf{H}\mathbf{x}^a + \boldsymbol{\varepsilon} \quad (2)$$

140 where  $\boldsymbol{\varepsilon}$  is an  $n \times 1$  vector of normally distributed noise with mean  $\boldsymbol{\varepsilon}_b$  and diagonal covariance matrix  
141  $\mathbf{R}$ :  $\boldsymbol{\varepsilon} \sim \mathcal{N}(\boldsymbol{\varepsilon}_b, \mathbf{R})$ . Our base case inversion assumes the mean bias is zero:  $\boldsymbol{\varepsilon}_b = \mathbf{0}$ . We evaluate the  
142 sensitivity to this assumption in Section 6 and Supplemental Section S5. These synthetic observa-  
143 tions can then be used in a Bayesian inference framework to estimate the optimal CO<sub>2</sub> fluxes (c.f.  
144 Rodgers, 2000). Assuming the prior and likelihood distributions are Gaussian gives us a closed-form  
145 solution for the posterior CO<sub>2</sub> fluxes:

$$146 \quad \hat{\mathbf{x}} = \mathbf{x}^b + (\mathbf{H}\mathbf{B})^T (\mathbf{H}\mathbf{B}\mathbf{H}^T + \mathbf{R})^{-1} (\mathbf{y}^a - \mathbf{H}\mathbf{x}^b) \quad (3)$$

147 where  $\mathbf{x}^b$  is an  $m \times 1$  vector of prior CO<sub>2</sub> fluxes, comprised of a coarse (10×10 km<sup>2</sup>) a-temporal  
148 EDGAR v4.2 FT2010 anthropogenic CO<sub>2</sub> inventory and natural fluxes from CarbonTracker CT2013B,  
149 regridded to 1×1 km<sup>2</sup>.  $\mathbf{B}$  is the  $m \times m$  prior error covariance matrix. The prior error covariance  
150 matrix can be expressed as a Kronecker product (cf. Meirink et al., 2008; Singh et al., 2011; Yadav  
151 and Michalak, 2013) of temporal and spatial covariance matrices:  $\mathbf{B} = \mathbf{D} \otimes \mathbf{E}$  where  $\mathbf{D}$  is the tem-  
152 poral covariance matrix and  $\mathbf{E}$  is the spatial covariance matrix. The  $\mathbf{B}$  matrix has an uncertainty of  
153 100% at the native resolution and the spatial and temporal covariance matrices are fully populated  
154 (see Supplemental Section S2 for more details).



155 We do not explicitly represent the individual error terms contributing to the  $\mathbf{R}$  matrix (instrument  
156 error, model error, and representation error). Instead, we have assumed that the  $\mathbf{R}$  matrix is diagonal  
157 and can be characterized by a single parameter: the total mismatch error ( $\sigma_m$ ;  $\mathbf{R} = \sigma_m^2 \mathbf{I}$ ), which  
158 represents the combined effects of the different error components.

159 Fig. 3 shows an example of the estimated  $\text{CO}_2$  fluxes. We can see that the posterior fluxes cap-  
160 ture more of the spatial variability in the  $\text{CO}_2$  fluxes than the prior fluxes in the region where the  
161 network is deployed. We find substantial improvements in the diurnal cycle (see panel d). Previ-  
162 ous work has used the posterior covariance matrix ( $\mathbf{Q} = (\mathbf{H}^T \mathbf{R}^{-1} \mathbf{H} + \mathbf{B}^{-1})^{-1}$ ), averaging kernel  
163 matrix ( $\mathbf{A} = \mathbf{I} - \mathbf{Q} \mathbf{B}^{-1}$ ), and the degrees of freedom for signal (DOFs =  $\text{tr}(\mathbf{A})$ ) as metrics to eval-  
164 uate the information content of different observing systems (e.g., Kort et al., 2013; Wu et al., 2015).  
165 However, it is computationally infeasible to construct these  $m \times m$  matrices for our application as  
166  $m > 10^6$  and storing them would require  $\sim 36$  Tb of memory (assuming double precision, dense  
167 matrices).

168 Instead, we evaluate the efficacy of the posterior fluxes by taking the norm of the difference be-  
169 tween the posterior fluxes and the true fluxes:  $\|\hat{\mathbf{x}} - \mathbf{x}^a\|_2$ . We express this as a relative improvement  
170 by comparing the norm of the difference between the prior fluxes and the true fluxes:

$$171 \quad \eta = 1 - \frac{\|\hat{\mathbf{x}} - \mathbf{x}^a\|_2}{\|\mathbf{x}^b - \mathbf{x}^a\|_2} \quad (4)$$

172 [Fig. 3 about here.]

173 This error metric,  $\eta$ , was chosen as it has a similar form to the averaging kernel matrix but it also  
174 allows us to directly compare the posterior fluxes to the true fluxes. This relative error metric can  
175 be related to the flux error (see Supplemental Section S4). As such, we can use the error metric to  
176 evaluate the ability of the observing system to resolve three types of emission sources: (1) area, (2)  
177 line, and (3) point sources, by examining a subset of grid cells in the domain (see Section S3 for  
178 more details). The area source (AS) examined here is the East Bay urban dome ( $147 \pm 55 \text{ tC hr}^{-1}$ ;  
179 uncertainty is the  $1\text{-}\sigma$  range of hourly fluxes from the high resolution inventory), the line source  
180 (LS) is Interstate 880 and the Bay Bridge ( $45 \pm 20 \text{ tC hr}^{-1}$ ), and the point sources (PS) are 4 large  
181  $\text{CO}_2$  sources in the East Bay ( $9 \pm 4 \text{ tC hr}^{-1}$ ). For comparison, Salt Lake City emits  $\sim 300 \pm 50 \text{ tC}$   
182  $\text{hr}^{-1}$  (McKain et al., 2012). The top panel of Fig. 2 shows these three source types.

183 Fig. 4 shows the error in the estimated  $\text{CO}_2$  fluxes using the observations over a wide range of  
184 observing system scenarios. We vary the number of sites ( $n_s$ ) and mismatch error ( $\sigma_m$ ) and perform  
185 an ensemble of 20 inversions for each combination to ensure the results are robust. Fig. 4 shows  
186 the mean error in the estimated  $\text{CO}_2$  fluxes for the area source, line source, and point source as a  
187 function of  $\sigma_m$  and  $n_s$ . This figure represents the uncertainty in the estimated emissions at a given  
188 hour.

189 [Fig. 4 about here.]



## 190 5 Simplified statistical models of error reduction

191 We develop statistical models to predict the error reduction and quantify the importance of the differ-  
192 ent factors governing the error reduction. We tested all combinations of models with the following  
193 7 parameters (127 possible combinations):  $\sqrt{\sigma_m}$ ,  $\sqrt{n_s}$ ,  $\ln(\sigma_m)$ ,  $\ln(n_s)$ ,  $\sigma_m$ ,  $n_s$ , and a constant.  
194 These statistical models were evaluated using Akaike information criterion (AIC) and Bayesian in-  
195 formation criterion (BIC). The following statistical models were found to be best:

$$196 \hat{\eta}_{AS} = \beta_6\sqrt{\sigma_m} + \beta_5\sqrt{n_s} + \beta_4\ln(\sigma_m) + \beta_3\ln(n_s) + \beta_2\sigma_m + \beta_0 \quad (5)$$

$$197 \hat{\eta}_{LS} = \beta_6\sqrt{\sigma_m} + \beta_5\sqrt{n_s} + \beta_4\ln(\sigma_m) + \beta_3\ln(n_s) + \beta_2\sigma_m + \beta_1n_s \quad (6)$$

$$198 \hat{\eta}_{PS} = \beta_6\sqrt{\sigma_m} + \beta_5\sqrt{n_s} + \beta_4\ln(\sigma_m) + \beta_2\sigma_m + \beta_0 \quad (7)$$

199 All the regression coefficients ( $\beta_i$ ) in the statistical models yielded statistically significant ( $p <$   
200 0.001) parameters based on F-tests (see the Supplemental Section S6 for the regression coefficients  
201 and model selection criterion).

202 We find the  $\sqrt{\sigma_m}$ ,  $\sqrt{n_s}$ ,  $\ln(\sigma_m)$ , and  $\sigma_m$  parameters in all three statistical models (Eq. 5–7).  
203 This dependence on  $\sqrt{n_s}$  and  $\sqrt{\sigma_m}$  logically follows from the assumption of Gaussian errors in  
204 the derivation of the posterior CO<sub>2</sub> fluxes (Eq. 3) and the basic properties of variance. These two  
205 parameters tend to be dominant and generally explain more than 50% of the variance. As such, we  
206 suspect that these two parameters are the most important and that other terms are capturing higher-  
207 order effects.

208 These statistical models can also be used to define the regimes where increasing the number of  
209 sites in the observing system is more important and those where reducing the mismatch error is more  
210 important by taking the derivative of  $\hat{\eta}$  with respect to  $n_s$ :

$$211 \frac{\partial \hat{\eta}_{AS}}{\partial n_s} = \frac{\beta_5}{2\sqrt{n_s}} + \frac{\beta_3}{n_s} \quad (8)$$

$$212 \frac{\partial \hat{\eta}_{LS}}{\partial n_s} = \frac{\beta_5}{2\sqrt{n_s}} + \frac{\beta_3}{n_s} + \beta_1 \quad (9)$$

$$213 \frac{\partial \hat{\eta}_{PS}}{\partial n_s} = \frac{\beta_5}{2\sqrt{n_s}} \quad (10)$$

214 From Fig. 4 we can see two distinct regimes: *noise-limited* and *site-limited*. Observing systems that  
215 lie above the  $\partial \hat{\eta} / \partial n_s$  curve are in the the noise-limited regime where the error reduction is largely  
216 governed by the mismatch error in the observing system. Conversely, observing systems below the  
217  $\partial \hat{\eta} / \partial n_s$  curve are in the the site-limited regime where the error reduction is largely governed by the  
218 number of sites in the observing system.

219 The mismatch error is controlled by the instrument, representation, and model error. In the noise-  
220 limited regime reducing these errors will provide the greatest benefit. Whereas, in the site-limited  
221 regime the greatest benefit will come from increasing the number of sites in the observing system  
222 and there will only be marginal benefit from reducing the instrument, representation, and model  
223 error.



## 224 6 Discussion

225 Three conclusions we can draw from Fig. 4 for California's East Bay are:

- 226 1. Achieving  $\sigma_m = 1$  ppm adds value. There is relatively little additional benefit to reducing  
227 mismatch error to 0.1 ppm, particularly for estimating line or point source emissions.
- 228 2. At  $\sigma_m = 1$  ppm there is a benefit to increasing the number of sites, but this benefit increases  
229 slower than  $\sqrt{n_s}$ .
- 230 3. At  $\sigma_m = 5$  ppm there is little benefit from increasing the number of sites; reducing the noise  
231 would add more value.

232 Our work is primarily focused on estimating hourly fluxes, however we can further reduce the  
233 uncertainty in our estimates by considering temporally averaged fluxes. Fig. 5 shows the error in  
234 our estimate of the area source emissions over various time-scales. We find the error in our estimate  
235 greatly decreases over the first 72 hours and agrees well with the error reduction predicted by the  
236 central limit theorem. This implies that our weekly-averaged emission estimate would be 10× better  
237 than our hourly emission estimate.

238 [Fig. 5 about here.]

### 239 6.1 Additional factors affecting observing system design

240 We considered three additional factors that could adversely impact an observing system: (1) inver-  
241 sion domain size, (2) site-specific systematic biases, and (3) using only daytime observations.

242 Our results are found to be largely insensitive to the inversion domain size (see Fig. S6). This is  
243 discerned through a set of sensitivity OSSEs with a reduced domain size. We find that inversions on  
244 the reduced domain were only marginally worse at reducing the error ( $\sim 1\%$ ) than inversions on the  
245 full domain (see Supplemental Section S5.1). This is due to the strong local signal in the footprint  
246 of the measurements (see bottom panel of Fig. 2). As such, the non-local emission sources do not  
247 adversely impact our ability to estimate urban emissions.

248 Biases can adversely impact the observing system (see Fig. S7). To test the impacts of biases in  
249 the modeling-measurement framework, we repeated the OSSEs outlined in Section 4 but included  
250 a systematic bias. The bias was unique to each site and was drawn from a normal distribution  
251 ( $\epsilon_b \sim \mathcal{N}(\mathbf{0}, \sigma_b^2 \mathbf{I})$ ;  $\sigma_b = 1$  ppm). There are three major findings from the OSSEs with systematic  
252 biases:

- 253 1. Systematic biases become particularly problematic when the spread of the potential biases  
254 (defined here as  $\sigma_b$ ) is larger than the mismatch error ( $\sigma_b > \sigma_m$ ). This is because we have  
255 defined the observational error covariance matrix as:  $\mathbf{R} = \sigma_m^2 \mathbf{I}$ . However, if  $\sigma_b > \sigma_m$  with a  
256 dense observing system then the site-specific biases will artificially inflate the observational



257 error covariance matrix:  $\mathbf{R} \approx (\sigma_m^2 + \sigma_b^2) \mathbf{I}$  and the errors will be incorrectly characterized in  
258 the observing system. As long as  $\sigma_b < \sigma_m$  then  $\mathbf{R} = \sigma_m^2 \mathbf{I}$  and the characterization of the errors  
259 will be appropriate.

260 2. Observing systems with more sites are generally less affected by site-specific systematic bi-  
261 ases. This is because observing systems with a small number of sites rely heavily on those few  
262 sites. An observing system with many sites is less reliant on a single site and the site-specific  
263 systematic biases act more like additional noise in the observing system.

264 3. Systematic biases have a greater impact when estimating an area source than line and point  
265 sources. This is because an air mass sensitive to a line or point source will have a greater  
266 enhancement relative to the background compared to a diffuse area source, thus there is a  
267 larger signal-to-noise ratio for these sources and a systematic bias is less important.

268 During the day, model calculations of the PBL height are more reliable leading to a temptation to  
269 omit the nighttime data from the analysis. However, emissions at night can be as much as 30% of  
270 the total and ignoring them makes estimates of urban emissions strongly dependent on prior assump-  
271 tions. Our observing system would be unable to correct the misrepresented nighttime emissions of  
272 our a-temporal prior without using nighttime observations. As a result, even our most optimistic  
273 observing system would have a systematic  $\sim 50$  tC hr<sup>-1</sup> error ( $\sim 30\%$ ) in the estimated area source  
274 emissions due to the misrepresented nighttime emissions.

## 275 6.2 Potential cost tradeoffs

276 We consider two potential observing systems:

277 1. “Network A” ( $n_s = 25$ ,  $\sigma_m = 1$  ppm): A dense network with moderate-precision instruments.  
278 This network is similar to the BEACO<sub>2</sub>N network described in Section 3. We assume a cost  
279 of \$5,000 per instrument giving a total cost of \$125,000. This network is shown as a purple  
280 star in the left column of Fig. 4.

281 2. “Network B” ( $n_s = 3$ ,  $\sigma_m = 0.1$  ppm): A sparse network with of high-precision instruments.  
282 This network uses cavity-ring down instruments. We assume a cost of \$50,000 per instrument  
283 giving a total cost of \$150,000. This network is shown as a green star in the left column of  
284 Fig. 4.

285 We note that the assumed mismatch error for these two potential observing systems is defined as the  
286 instrument error and assumes there is no contribution from model or transport errors.

287 The cost for these two networks is comparable. From Fig. 4, we find that the sparse “Network B”  
288 is site-limited in all cases whereas the dense “Network A” is near the noise/site-limited boundary.  
289 Further, we find that the dense “Network A” has less error in the estimate of all source types in San



290 Francisco's East Bay. Networks sitting exactly on the ridge line are at the optimal balance between  
291 precision and number of sites.

### 292 6.3 The relationship between network density and transport error

293 In this work we have treated transport error and the number of measurement sites as independent.  
294 However, in practice, there would be a relationship between the transport error and measurement  
295 network density. This can be understood with a thought experiment using two different observing  
296 systems to estimate emissions: a sparse network with a single site and an infinitely dense network  
297 (sites at each grid cell in our domain). Estimating emissions with the sparse network would require  
298 us to simulate the atmospheric transport with high fidelity if we are to reliably say anything about  
299 emissions upwind of our site. This is especially true for point sources. Any errors in the simulated  
300 atmospheric transport would adversely impact the estimated emissions, whereas the infinitely dense  
301 network could potentially neglect atmospheric transport and use data from only the local grid cell  
302 to estimate emissions. This is because the differential signal at each site would be largely gov-  
303 erned by the local emissions. Explicitly quantifying this relationship between transport error and  
304 measurement network density should be the focus of future work.

## 305 7 Conclusions

306 Understanding the factors that govern our ability to estimate urban greenhouse gas emissions are  
307 crucial to improving an observing system and reducing the uncertainty in emission estimates. Here  
308 we have quantitatively mapped the errors in CO<sub>2</sub> emission estimates from different observing sys-  
309 tems for three different types of sources in California's Bay Area: area sources, line sources, and  
310 point sources. Our results show that different observing systems may fall into noise or site-limited  
311 regimes where reducing the uncertainty in the estimated emissions is governed by a single factor;  
312 these regimes differ for the source types. Identifying the regime an observing system is in will help  
313 inform future improvements to the observing system. A number of prior urban CO<sub>2</sub> experiments  
314 have defined as a goal, the understanding of emissions to less than 10% (e.g., Kort et al., 2013; Wu  
315 et al., 2015). We find that a BEACO<sub>2</sub>N-like network could achieve this accuracy and precision with  
316 1 week of observations, if the dominant source of error is instrument precision. This conclusion may  
317 motivate a re-examining of the conventional instrument quality-oriented design of CO<sub>2</sub> observing  
318 systems, according to the stated goal of a given network.

319 *Acknowledgements.* This work was supported by a Department of Energy (DOE) Computational Science Grad-  
320 uate Fellowship (CSGF) to AJT, a National Science Foundation (NSF) Grant 1035050 to RCC, and a Bay Area  
321 Air Quality Management District (BAAQMD) Grant 2013.145 to RCC. AAS was supported by a National Sci-  
322 ence Foundation Graduate Research Fellowship. This research used resources of the National Energy Research  
323 Scientific Computing Center, which is supported by the Office of Science of the U.S. Department of Energy



324 under Contract No. DE-AC02-05CH11231. We thank M. Sulprizio (Harvard University) for gridding the US  
325 Census population data and the UC Berkeley Academic Computing center for access to computing resources.



326 **References**

- 327 Breon, F. M., Broquet, G., Puygrenier, V., Chevallier, F., Xueref-Remy, I., Ramonet, M., Dieudonn, E.,  
328 Lopez, M., Schmidt, M., Perrussel, O., and Ciais, P.: An attempt at estimating Paris area CO<sub>2</sub> emissions  
329 from atmospheric concentration measurements, *Atmospheric Chemistry and Physics*, 15, 1707–1724, doi:  
330 10.5194/acp-15-1707-2015, 2015.
- 331 Deschênes, O. and Greenstone, M.: Climate Change, Mortality, and Adaptation: Evidence from Annual  
332 Fluctuations in Weather in the US, *American Economic Journal: Applied Economics*, 3, 152–185, doi:  
333 10.1257/app.3.4.152, 2011.
- 334 EIA, U.: Emissions of Greenhouse Gases in the U.S., Tech. rep., U.S. Energy Information Administration,  
335 2015.
- 336 European Commission: Emission Database for Global Atmospheric Research (EDGAR), release version 4.2,  
337 Tech. rep., Joint Research Centre (JRC)/Netherlands Environmental Assessment Agency (PBL), 2011.
- 338 Gately, C. K., Hutyra, L. R., Wing, I. S., and Brondfield, M. N.: A bottom up approach to on-road CO<sub>2</sub>  
339 emissions estimates: improved spatial accuracy and applications for regional planning, *Environ Sci Technol*,  
340 47, 2423–30, doi:10.1021/es304238v, 2013.
- 341 Gately, C. K., Hutyra, L. R., and Sue Wing, I.: Cities, traffic, and CO<sub>2</sub>: A multidecadal assessment of  
342 trends, drivers, and scaling relationships, *Proc Natl Acad Sci U S A*, 112, 4999–5004, doi:10.1073/pnas.  
343 1421723112, 2015.
- 344 Gratani, L. and Varone, L.: Daily and seasonal variation of CO in the city of Rome in relationship with the  
345 traffic volume, *Atmospheric Environment*, 39, 2619–2624, doi:10.1016/j.atmosenv.2005.01.013, 2005.
- 346 Gurney, K. R., Mendoza, D. L., Zhou, Y., Fischer, M. L., Miller, C. C., Geethakumar, S., and de la Rue du Can,  
347 S.: High resolution fossil fuel combustion CO<sub>2</sub> emission fluxes for the United States, *Environ Sci Technol*,  
348 43, 5535–41, 2009.
- 349 Gurney, K. R., Razlivanov, I., Song, Y., Zhou, Y., Benes, B., and Abdul-Massih, M.: Quantification of fossil  
350 fuel CO<sub>2</sub> emissions on the building/street scale for a large U.S. city, *Environ Sci Technol*, 46, 12 194–202,  
351 doi:10.1021/es3011282, 2012.
- 352 Hutyra, L. R., Duren, R., Gurney, K. R., Grimm, N., Kort, E. A., Larson, E., and Shrestha, G.: Urbanization  
353 and the carbon cycle: Current capabilities and research outlook from the natural sciences perspective, *Earth's*  
354 *Future*, 2, 473–495, doi:10.1002/2014ef000255, 2014.
- 355 IPCC: Climate Change 2013: The Physical Science Basis. Contribution of Working Group I to the Fifth As-  
356 sessment Report of the Intergovernmental Panel on Climate Change, Tech. rep., 2013.
- 357 Kort, E. A., Angevine, W. M., Duren, R., and Miller, C. E.: Surface observations for monitoring urban fossil fuel  
358 CO<sub>2</sub> emissions: Minimum site location requirements for the Los Angeles megacity, *Journal of Geophysical*  
359 *Research: Atmospheres*, 118, 1577–1584, doi:10.1002/jgrd.50135, 2013.
- 360 Lauvaux, T., Miles, N. L., Richardson, S. J., Deng, A., Stauffer, D. R., Davis, K. J., Jacobson, G., Rella, C.,  
361 Calonder, G.-P., and DeCola, P. L.: Urban Emissions of CO<sub>2</sub> from Davos, Switzerland: The First Real-  
362 Time Monitoring System Using an Atmospheric Inversion Technique, *Journal of Applied Meteorology and*  
363 *Climatology*, 52, 2654–2668, doi:10.1175/jamc-d-13-038.1, 2013.
- 364 Lin, J. C., Gerbig, C., Wofsy, S. C., Andrews, A. E., Daube, B. C., Davis, K. J., and Grainger, C. A.: A near-  
365 field tool for simulating the upstream influence of atmospheric observations: The Stochastic Time-Inverted



- 366 Lagrangian Transport (STILT) model, *Journal of Geophysical Research-Atmospheres*, 108, ACH 2–1–ACH  
367 2–17, doi:10.1029/2002jd003161, 2003.
- 368 Mangat, T. S., Claire, S. J., Dinh, T. M., Fanai, A. K., Nguyen, M. H., and Schultz, S. A.: Source inventory of  
369 Bay Area greenhouse gas emissions, Tech. rep., Bay Area Air Quality Management District, 2010.
- 370 McDonald, B. C., McBride, Z. C., Martin, E. W., and Harley, R. A.: High-resolution mapping of motor vehicle  
371 carbon dioxide emissions, *Journal of Geophysical Research-Atmospheres*, 119, 5283–5298, doi:10.1002/  
372 2013jd021219, 2014.
- 373 McKain, K., Wofsy, S. C., Nehr Korn, T., Eluszkiewicz, J., Ehleringer, J. R., and Stephens, B. B.: Assessment of  
374 ground-based atmospheric observations for verification of greenhouse gas emissions from an urban region,  
375 *Proc Natl Acad Sci U S A*, 109, 8423–8, doi:10.1073/pnas.1116645109, 2012.
- 376 Meirink, J. F., Bergamaschi, P., and Krol, M. C.: Four-dimensional variational data assimilation for inverse  
377 modelling of atmospheric methane emissions: method and comparison with synthesis inversion, *Atmo-  
378 spheric Chemistry and Physics*, 8, 6341–6353, doi:10.5194/acp-8-6341-2008, 2008.
- 379 Nassar, R., Napier-Linton, L., Gurney, K. R., Andres, R. J., Oda, T., Vogel, F. R., and Deng, F.: Improving  
380 the temporal and spatial distribution of CO<sub>2</sub> emissions from global fossil fuel emission data sets, *Journal of  
381 Geophysical Research: Atmospheres*, 118, 917–933, doi:10.1029/2012jd018196, 2013.
- 382 Nehr Korn, T., Eluszkiewicz, J., Wofsy, S. C., Lin, J. C., Gerbig, C., Longo, M., and Freitas, S.: Coupled weather  
383 research and forecasting stochastic time-inverted lagrangian transport (WRF–STILT) model, *Meteorology  
384 and Atmospheric Physics*, 107, 51–64, doi:10.1007/s00703-010-0068-x, 2010.
- 385 Newman, S., Jeong, S., Fischer, M. L., Xu, X., Haman, C. L., Lefer, B., Alvarez, S., Rappenglueck, B., Kort,  
386 E. A., Andrews, A. E., Peischl, J., Gurney, K. R., Miller, C. E., and Yung, Y. L.: Diurnal tracking of anthro-  
387 pogenic CO<sub>2</sub> emissions in the Los Angeles basin megacity during spring 2010, *Atmospheric Chemistry and  
388 Physics*, 13, 4359–4372, doi:10.5194/acp-13-4359-2013, 2013.
- 389 Oda, T. and Maksyutov, S.: A very high-resolution (1 km×1 km) global fossil fuel CO<sub>2</sub> emission inventory  
390 derived using a point source database and satellite observations of nighttime lights, *Atmospheric Chemistry  
391 and Physics*, 11, 543–556, doi:10.5194/acp-11-543-2011, 2011.
- 392 Peters, W., Jacobson, A. R., Sweeney, C., Andrews, A. E., Conway, T. J., Masarie, K., Miller, J. B., Bruhwiler,  
393 L. M., Petron, G., Hirsch, A. I., Worthy, D. E., van der Werf, G. R., Randerson, J. T., Wennberg, P. O.,  
394 Krol, M. C., and Tans, P. P.: An atmospheric perspective on North American carbon dioxide exchange:  
395 CarbonTracker, *Proc Natl Acad Sci U S A*, 104, 18 925–30, doi:10.1073/pnas.0708986104, 2007.
- 396 Rigby, M., Toumi, R., Fisher, R., Lowry, D., and Nisbet, E. G.: First continuous measurements of CO<sub>2</sub> mixing  
397 ratio in central London using a compact diffusion probe, *Atmospheric Environment*, 42, 8943–8953, doi:  
398 10.1016/j.atmosenv.2008.06.040, 2008.
- 399 Rodgers, C. D.: *Inverse Methods for Atmospheric Sounding*, World Scientific, Singapore, 2000.
- 400 Singh, K., Jardak, M., Sandu, A., Bowman, K., Lee, M., and Jones, D.: Construction of non-diagonal back-  
401 ground error covariance matrices for global chemical data assimilation, *Geoscientific Model Development*,  
402 4, 299–316, doi:10.5194/gmd-4-299-2011, 2011.
- 403 Turnbull, J. C., Sweeney, C., Karion, A., Newberger, T., Lehman, S. J., Tans, P. P., Davis, K. J., Lauvaux, T.,  
404 Miles, N. L., Richardson, S. J., Cambaliza, M. O., Shepson, P. B., Gurney, K., Patarasuk, R., and Razlivanov,  
405 I.: Toward quantification and source sector identification of fossil fuel CO<sub>2</sub> emissions from an urban area:



- 406 Results from the INFLUX experiment, *Journal of Geophysical Research-Atmospheres*, 120, 292–312, doi:  
407 10.1002/2014JD022555, 2015.
- 408 Wu, L., Broquet, G., Ciais, P., Bellassen, V., Vogel, F., Chevallier, F., Xueref-Remy, I., and Wang, Y.: Atmo-  
409 spheric inversion for cost effective quantification of city CO<sub>2</sub> emissions, *Atmospheric Chemistry and Physics*  
410 *Discussions*, 15, 30 693–30 756, doi:10.5194/acpd-15-30693-2015, 2015.
- 411 Yadav, V. and Michalak, A. M.: Improving computational efficiency in large linear inverse problems:  
412 an example from carbon dioxide flux estimation, *Geoscientific Model Development*, 6, 583–590, doi:  
413 10.5194/gmd-6-583-2013, 2013.

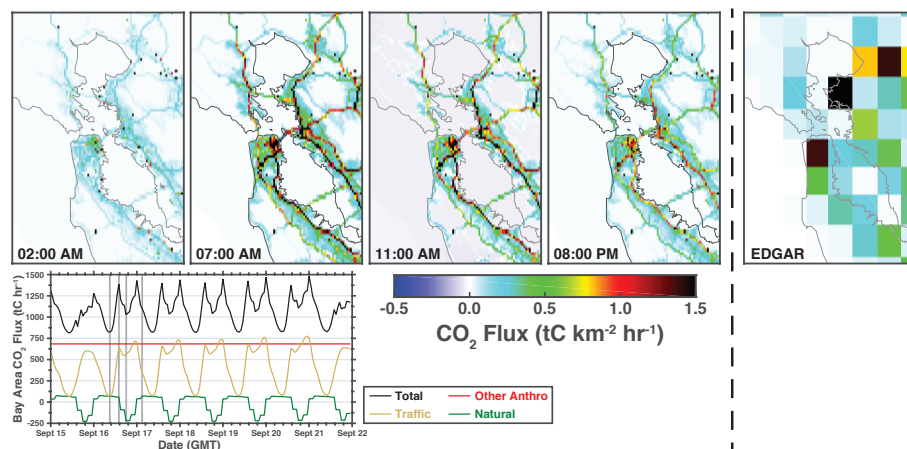


**Fig. 1.** September 2013 CO<sub>2</sub> fluxes from bottom-up inventories. Top row shows the fluxes in the Bay Area (122.0357° – 122.7683°W, 37.3771° – 38.2218°N) at four representative hours (hour in local time). Right panel shows the a-temporal EDGAR v4.2 FT2010 CO<sub>2</sub> flux in the Bay Area. Bottom panel shows the total Bay Area CO<sub>2</sub> flux (black), traffic (orange), other anthropogenic (red), and natural (green) sources. Vertical gray shading indicates the time slices plotted in the top and middle panels.

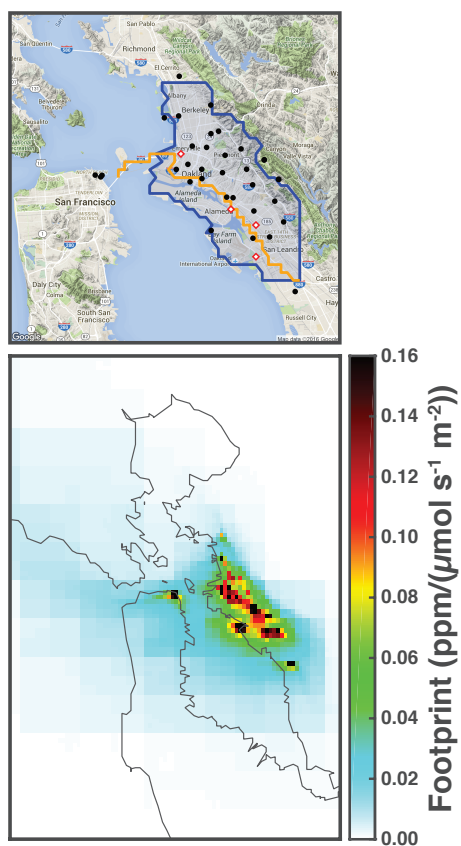


**Fig. 2.** Top panel shows the location of the sites (black circles), the area source (blue region), the line source (orange line), and point sources (red diamonds). Bottom panel shows the September 15 to 22 average footprint for the 34 sites in the network, see Table 1 for a list of the sites. The bottom panel is the full domain used for the inversion.

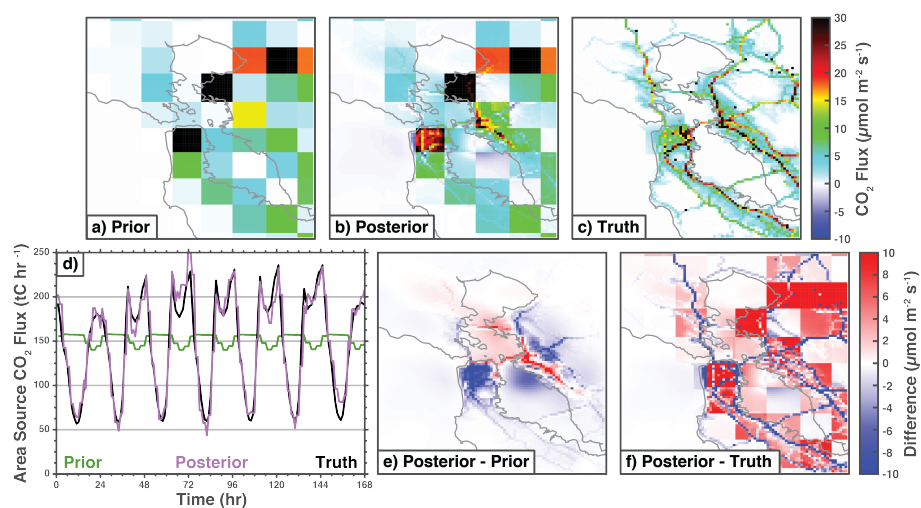


**Fig. 3.** Example of estimated CO<sub>2</sub> fluxes. Top row shows the average emissions from (a) the prior, (b) the posterior, and (c) the true emissions. Panel (d) shows a time series of the emissions from the area source with the prior (green), posterior (pink), and true emissions (black). Panel (e) shows the difference between the posterior and the prior. Panel (f) shows the difference between posterior and the truth. Posterior output is from the best case scenario ( $n_S = 34$  and  $\sigma_m = 0.005$  ppm).

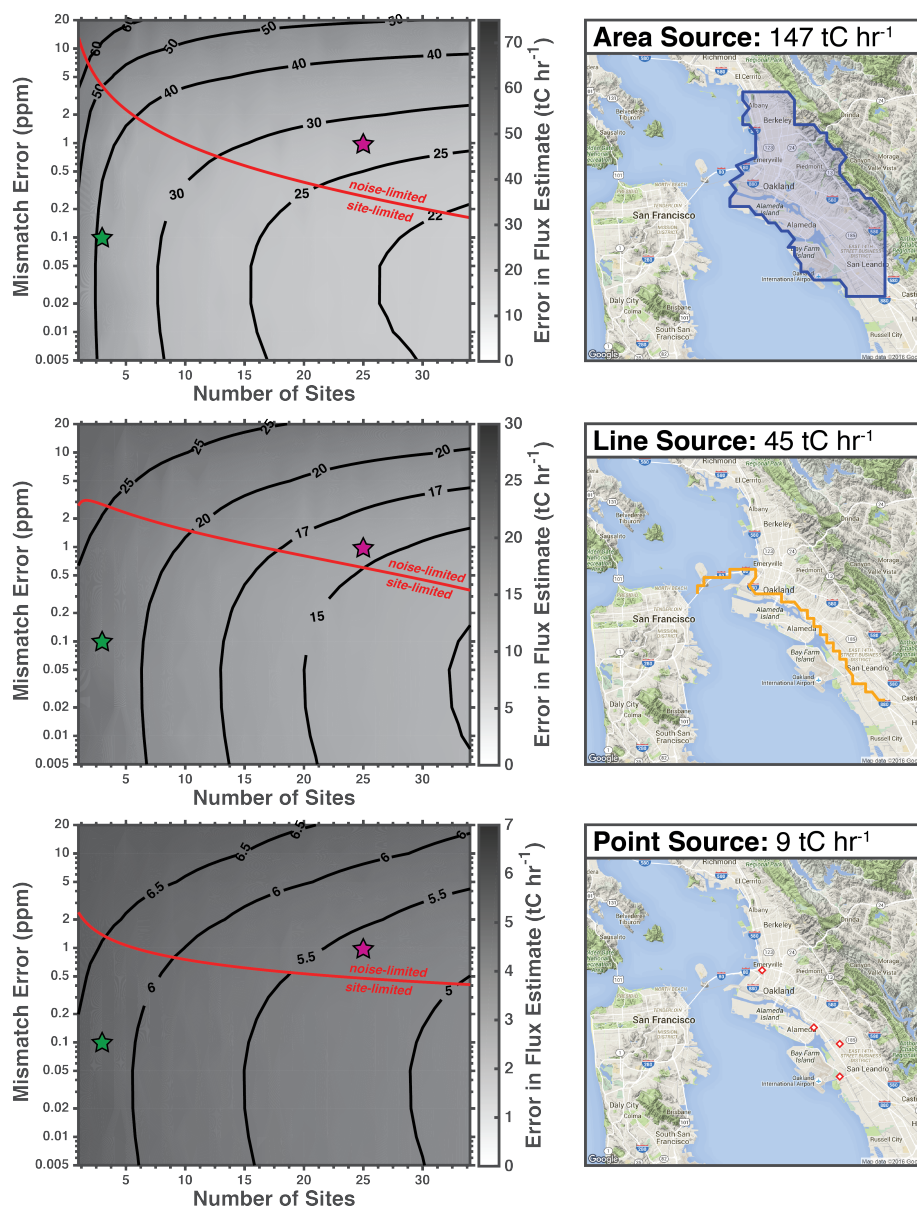


**Fig. 4.** Left column shows the error in the posterior CO<sub>2</sub> fluxes. Right column shows the fluxes being estimated. Top row is the area source, middle row is the line source, and bottom row is the point source. Results are the mean of a monte carlo analysis using 20 different combinations of sites. Contours are from the statistical models  $\hat{\eta}$  (see Eq. 5–7) converted to flux errors and the red lines are the partial derivative of the statistical models with respect to the number of sites,  $\partial\hat{\eta}/\partial n_s$  (Eq. 8–10), that define the cutoff between the noise-limited and site-limited regimes. Purple star shows an observing system with 25 sites and 1 ppm noise. Green star shows an observing system with 3 sites and 0.1 ppm noise. Note the log-scale on the y-axis.



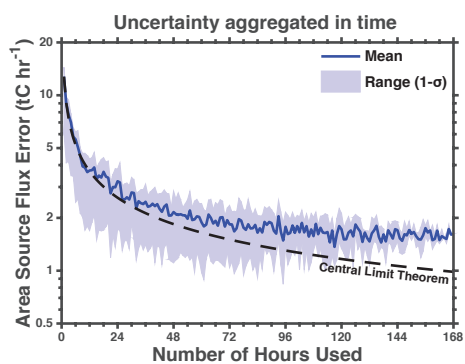


**Fig. 5.** Uncertainty aggregated in time for the best case inversion (see Fig. 3). The CO<sub>2</sub> flux estimate in this study has an hourly temporal resolution. The uncertainty in the emissions estimate declines as the estimate is averaged to longer temporal scales. Solid blue line is the mean uncertainty, shading is the 1- $\sigma$  range, and the dashed black line is the uncertainty predicted by the central limit theorem. Note the log scale on the y-axis.

**Table 1.** 34 sites in the network<sup>a</sup> used in this study.

Site Code	Site name	Latitude (°N)	Longitude (°W)	Height (m a.g.l.)
AHS	Arroyo High School	37.680	122.139	3
BEL	Burckhalter Elementary School	37.775	122.167	5
BFE	Bayfarm Elementary School	37.744	122.251	3
BOD	Bishop O'Dowd High School	37.753	122.155	3
CES	Claremont Elementary School	37.846	122.252	3
CHA	Chabot Space & Science Center (low)	37.819	122.181	3
CHB	Chabot Space & Science Center (high)	37.819	122.181	9
COI	Coit Tower	37.8030	122.406	5
CPS	College Preparatory School	37.849	122.242	24
EBM	W. Oakland EBMUD Monitoring Station	37.814	122.282	3
ELC	El Cerrito High School	37.907	122.294	8
EXB	Exploratorium (Bay)	37.803	122.397	6
EXE	Exploratorium (Embarcadero)	37.801	122.399	3
FTK	Fred T. Korematsu Discovery Academy	37.738	122.174	3
GLE	Greenleaf Elementary School	37.765	122.194	3
HRS	Head Royce School	37.809	122.204	7
ICS	International Community School	37.779	122.231	3
KAI	Kaiser Center	37.809	122.264	127
LAU	Laurel Elementary School	37.792	122.197	12
LBL	Lawrence Berkeley National Lab, Bldg. 70	37.876	122.252	3
LCC	Lighthouse Community Charter School	37.736	122.196	3
MAR	Berkeley Marina	37.863	122.314	3
MON	Montclair Elementary School	37.830	122.212	3
NOC	N. Oakland Community Charter School	37.833	122.277	3
OMC	Oakland Museum of California	37.799	122.264	3
PAP	PLACE at Prescott Elementary	37.809	122.298	3
PDS	Park Day School	37.832	122.257	3
PHS	Piedmont Middle & High School	37.824	122.233	3
POR	Port of Oakland Headquarters	37.796	122.280	3
OHS	Oakland High School	37.805	122.236	3
ROS	Rosa Parks Elementary School	37.865	122.295	3
SHA	Skyline High School (low)	37.798	122.162	3
SHB	Skyline High School (high)	37.798	122.162	13
STL	St. Elizabeth High School	37.779	122.222	3

<sup>a</sup> This study uses both operational and proposed sites. See here for more information on the network: "<http://beacon.berkeley.edu/>".